Homoclinic orbits in the Maxwell-Bloch equations with a probe

Darryl D. Holm

Theoretical Division, Los Alamos National Laboratory, Los Alamos, New Mexico 87545

Gregor Kovačič and Thomas A. Wettergren[*]

Mathematical Sciences Department, Rensselaer Polytechnic Institute, Troy, New York 12180

The dynamics of an ensemble of two-level atoms in a single-mode resonant laser cavity with external pumping and a weak coherent probe is investigated. The system is represented as a perturbation to an integrable system, the Jaynes-Cummings model, in which there are no losses. Using an analytical perturbation technique, the Melnikov method, we show the presence of special homoclinic orbits, which persist under small perturbation from the homoclinic structure present in the integrable case on codimension-one surfaces in the parameter space. Two cases are considered: one in which we consider the equations with small relaxation parameters and no probe and the second in which we consider the small relaxation parameters and the effects of the probe. The persistence of homoclinic orbits for larger parameters is demonstrated through numerical continuation using the software package AUTO. The breakup of these homoclinic orbits is believed to be a source of chaos in the laser system. [S1063-651X(96)02307-0]

PACS number(s): 05.45.+b, 42.65.Sf

I. INTRODUCTION

The Maxwell-Bloch equations for single-mode laser operation [1–4] invite a dynamical systems approach, especially because they contain the famous Lorenz equations as a subsystem. Dynamical systems ideas, while not necessarily complete from the viewpoint of physics, at least provide an organizing principle for investigations of laser dynamics. For example, Arecchi [4] and Weiss [5] review and evaluate the experimental observability of some of the behavior of laser operation that is interesting from a dynamical systems viewpoint.

The dynamical systems approach we take is intended to map out the regions in the parameter space for single-mode laser operation where interesting dynamical behavior will take place, provided the dynamics can indeed be described by the Maxwell-Bloch equations. In order for these equations to apply, we must assume the laser to be an ensemble of two-level atoms in a single-mode resonant cavity with external pumping. We must also assume that the sample of lasing material in the cavity is small enough that we can neglect all spatial effects. Finally, the Maxwell-Bloch equations ignore quantum effects in the electric field. If we denote the complex envelopes of the electric field by $\mathcal{E}$, the medium polarizability by $\mathcal{P}$, and the real-valued population inversion by $\mathcal{D}$, the Maxwell-Bloch equations read

$$\dot{\mathcal{E}} = \mathcal{P} - \varepsilon\alpha\mathcal{E}, \tag{1.1a}$$

$$\dot{\mathcal{P}} = \mathcal{E}\mathcal{D} - \varepsilon\beta\mathcal{P}, \tag{1.1b}$$

$$\dot{\mathcal{D}} = -\tfrac{1}{2}(\mathcal{E}\mathcal{P}^* + \mathcal{E}^*\mathcal{P}) - \varepsilon\gamma(\mathcal{D}-1), \tag{1.1c}$$

where the overdot denotes the time derivative. Here the parameter $\varepsilon\alpha$ represents the cavity losses, while $\varepsilon\beta$ and $\varepsilon\gamma$ are the parallel and perpendicular relaxation rates for the lasing material in the cavity, respectively, and ε is the inverse of the coupling constant. These equations assume comparable time scales for the processes of cavity damping $\varepsilon\alpha$ and the relaxation of atomic states $\varepsilon\beta$ and $\varepsilon\gamma$.

If a small-amplitude, slightly detuned probe is injected into the laser cavity, the Maxwell-Bloch equations become [6,7]

$$\dot{\mathcal{E}} = \mathcal{P} - \varepsilon\alpha\mathcal{E}, \tag{1.2a}$$

$$\dot{\mathcal{P}} = (\mathcal{E} + \varepsilon\delta e^{i\omega t})\mathcal{D} - \varepsilon\beta\mathcal{P}, \tag{1.2b}$$

$$\dot{\mathcal{D}} = -\frac{1}{2}\left[(\mathcal{E} + \varepsilon\delta e^{i\omega t})\mathcal{P}^* + (\mathcal{E}^* + \varepsilon\delta e^{-i\omega t})\mathcal{P}\right]$$
$$- \varepsilon\gamma(\mathcal{D}-1), \tag{1.2c}$$

where $\varepsilon\delta$ is the strength of the probe laser and ω is the detuning between the frequencies of the probe light and the radiation in the resonant cavity, which is tuned to match the atomic transition frequency. All the variables and parameters are dimensionless; their dimensional counterparts are discussed, for instance, in [7]. An idealized experimental setup showing the laser cavity, together with the weak coherent probe, is depicted in Fig. 1.

The type of dynamical systems behavior we are seeking is the persistence or breakup of homoclinic orbits as the parameters $\varepsilon\alpha$, $\varepsilon\beta$, $\varepsilon\gamma$, and $\varepsilon\delta$ are varied. We find persisting homoclinic orbits in two ways: by the Melnikov method, as reviewed in [8], and by numerical continuation using the computer code AUTO [9]. Our investigation yields a fairly complete picture of the surface in the $\varepsilon\alpha$-$\varepsilon\beta$-$\varepsilon\gamma$-$\varepsilon\delta$ parameter space where certain homoclinic orbits exist that are believed to be responsible for the occurrence of chaotic dynam-

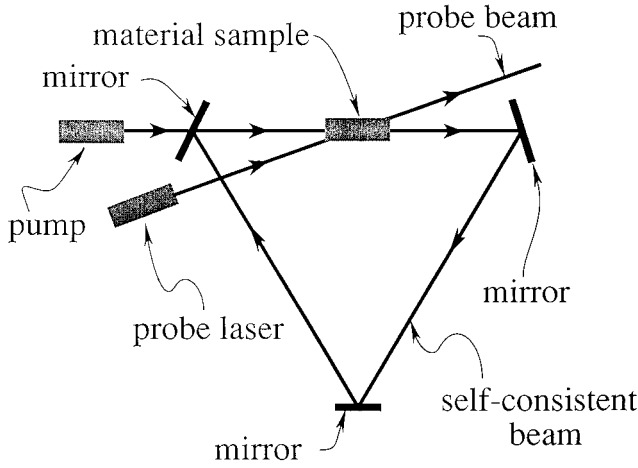*Present address: Naval Undersea Warfare Center, Code 8423, Newport, RI 02841.

FIG. 1. Diagram of the ring-cavity laser system with an external probe laser and an external pump. We assume that the lasing sample is short enough so that spatial effects can be ignored and that a two-level description is sufficient.

ics [10,11]. For small values of ε, this surface is well approximated by its tangent space at the origin, which is calculated by the Melnikov method. Moreover, this surface contains all previously discovered cases of the same type of homoclinic orbits. Varying the parameters away from this surface leads to bifurcations of various kinds that have been well studied for the Lorenz system [11]. We propose a different bifurcation path that may be suitable for laser optics.

In Sec. II we describe the dynamics of the integrable case, which we obtain by setting $\varepsilon=0$. In Sec. III we derive the conditions on the parameters $\varepsilon\alpha$, $\varepsilon\beta$, and $\varepsilon\gamma$ for homoclinic orbits to persist under perturbation in the case when the perturbation contains no probe and also map out numerically using the code AUTO [9] the two-dimensional surface in the $\varepsilon\alpha$-$\varepsilon\beta$-$\varepsilon\gamma$ parameter space on which these homoclinic orbits persist as $\varepsilon\alpha$, $\varepsilon\beta$, and $\varepsilon\gamma$ increase to finite values. The continuation method we use tracks the same homoclinic orbit as the parameters increase along a continuous locus in parameter space that has two branches. Section IV reviews the comparison with the Lorenz equations and laser experiments. Section V treats a Smale horseshoe construction that leads to chaotic dynamics. Section VI treats the effects of injection of a low-intensity, slightly detuned probe laser into the original laser cavity. The injection of the probe laser introduces two other phases into the problem and thus raises the dimension of the laser dynamical system from 3 to 5. The additional degrees of freedom complicate the discussion technically, but the basic structure of the parameter space and the features of the bifurcations to a strange attractor are very similar to those in the case without the probe.

II. THE INTEGRABLE CASE

A. Integrable limit and conservation laws

In the limit as ε goes to zero in Eqs. (1.2), we recover the integrable Hamiltonian equations of the classical Jaynes-Cummings model [12]. This integrable limit corresponds to absence of the probe and neglect of cavity losses and relaxation in the medium. In this limit, the Maxwell-Bloch equations read

$$\dot{\mathcal{E}}=\mathcal{P}, \tag{2.1a}$$

$$\dot{\mathcal{P}}=\mathcal{E}\mathcal{D}, \tag{2.1b}$$

$$\dot{\mathcal{D}}=-\tfrac{1}{2}(\mathcal{E}\mathcal{P}*+\mathcal{E}*\mathcal{P}). \tag{2.1c}$$

These equations possess three conserved quantities: unitarity

$$H=\tfrac{1}{2}|\mathcal{P}|^2+\tfrac{1}{2}\mathcal{D}^2, \tag{2.2}$$

the interaction energy

$$J=\frac{1}{2i}(\mathcal{E}\mathcal{P}*-\mathcal{E}*\mathcal{P}), \tag{2.3}$$

and the sum of the electric field energy and the excitation energy

$$K=\tfrac{1}{2}|\mathcal{E}|^2+\mathcal{D}. \tag{2.4}$$

Eliminating the population inversion $\mathcal{D}$ in favor of the energy K in Eqs. (2.1) yields the ideal complex Duffing system

$$\dot{\mathcal{E}}=\mathcal{P}, \quad \dot{\mathcal{P}}=\mathcal{E}(K-\tfrac{1}{2}|\mathcal{E}|^2). \tag{2.5}$$

The unitarity H serves as the Hamiltonian for these equations, namely,

$$\dot{\mathcal{E}}=2\frac{\partial H}{\partial \mathcal{P}*}, \quad \dot{\mathcal{P}}=-2\frac{\partial H}{\partial \mathcal{E}*},$$

with

$$H=\tfrac{1}{2}|\mathcal{P}|^2+\tfrac{1}{2}(K-\tfrac{1}{2}|\mathcal{E}|^2)^2. \tag{2.6}$$

B. Homoclinic orbits in five dimensions

In previous work [13,14], the authors showed that there exist homoclinic orbits in Eqs. (2.5), which are given explicitly by

$$\mathcal{E}=2\sqrt{K}\ \text{sech}(\sqrt{K}t)e^{i\theta},$$

$$\mathcal{P}=-2K\ \text{sech}(\sqrt{K}t)\tanh(\sqrt{K}t)e^{i\theta}, \tag{2.7}$$

where θ is a time-independent phase angle. Solutions (2.7) are homoclinic to the equilibrium at $\mathcal{E}=\mathcal{P}=0$, $K>0$. This equilibrium corresponds to the absence of any cavity radiation and material polarizability, with all of the atoms of the material sample being in the completely inverted state. (Polarizability vanishes in this state because there is no charge separation to form an atomic dipole moment.) The curve of completely-inverted-state equilibria at $\mathcal{E}=\mathcal{P}=0$, $K>0$ is connected to itself by a parametrized family of two-dimensional homoclinic tori, given by the solutions (2.7) or implicitly by

$$H-\tfrac{1}{2}K^2=0, \quad J=0. \tag{2.8}$$

This family of homoclinic tori is shown schematically in Fig. 2. Each torus describes the locus of states undergone by the system as the material emits light into the cavity and reabsorbs it in infinite time. The aim of this paper is to use this
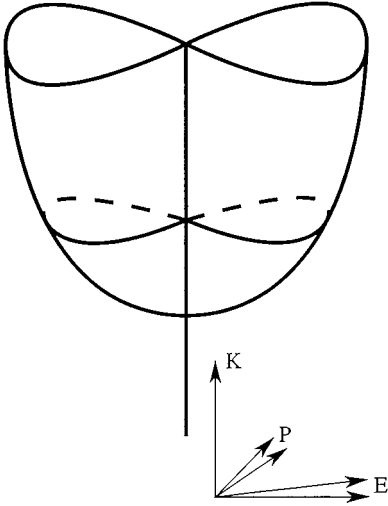
FIG. 2. Sketch of the homoclinic manifold for the integrable system. Each K level of this is a pinched two-dimensional torus filled with orbits homoclinic to the equilibrium at $(\mathcal{E},\mathcal{P},K) = (0,0,K)$.

family of homoclinic tori as a framework in which to analyze the chaotic behavior of Eqs. (1.2).

III. THE CASE WITH NO PROBE

A. An attracting family of real subsystems

Equations (1.1), which describe the ring-laser cavity in the absence of the probe laser, possess a circular symmetry. In particular, they are invariant under the transformation $(\mathcal{E},\mathcal{P})\mapsto(\mathcal{E}e^{i\phi},\mathcal{P}e^{i\phi})$ for any real ϕ. By writing $\mathcal{E}e^{i\phi}$ and $\mathcal{P}e^{i\phi}$ with real $\mathcal{E}$ and $\mathcal{P}$ instead of the usual complex $\mathcal{E}$ and $\mathcal{P}$, we find that $d\phi/dt = 0$. Therefore, Eqs. (1.2) with $\delta=0$ contain a continuous family of real subsystems

$$\dot{\mathcal{E}} = \mathcal{P} - \varepsilon\alpha\mathcal{E}, \tag{3.1a}$$

$$\dot{\mathcal{P}} = \mathcal{E}(K - \tfrac{1}{2}\mathcal{E}^2) - \varepsilon\beta\mathcal{P}, \tag{3.1b}$$

$$\dot{K} = -\varepsilon\alpha\mathcal{E}^2 - \varepsilon\gamma(K - \tfrac{1}{2}\mathcal{E}^2 - 1), \tag{3.1c}$$

which are parametrized by the phase ϕ. In Eqs. (3.1) the inversion $\mathcal{D}$ has been eliminated in favor of the energy K given by Eq. (2.4). This continuous family of real subsystems is precisely the subspace of the complex $\mathcal{E}$-$\mathcal{P}$-K phase space in which $J=0$. Equations (1.1) imply

$$\dot{J} = -\varepsilon(\alpha+\beta)J.$$

Hence the $J=0$ subspace is attracting and is therefore the only submanifold of importance in the long-time behavior of the system [15].

B. The ideal limit

When $\varepsilon=0$, the $\mathcal{E}$-$\mathcal{P}$ dynamics is governed by a parametrized family of ideal Duffing oscillators. In the full $\mathcal{E}$-$\mathcal{P}$-K phase space, the points $\mathcal{E}=\mathcal{P}=0$ with $K>0$ form a hyper-

bolic line of equilibria that is connected to itself by a two-sheeted homoclinic manifold similar to that shown in Fig. 2. This manifold is just the collection of all the pairs of separatrices that connect the origin $\mathcal{E}=\mathcal{P}=0$ to itself on each constant K slice. These manifolds are parametrized by t and K in the homoclinic solutions (2.7) with $\theta=0$ and $\theta=\pi$, namely,

$$\mathcal{E} = \pm 2\sqrt{K}\ \text{sech}(\sqrt{K}t), \quad \mathcal{P} = \mp 2K\ \text{sech}(\sqrt{K}t)\tanh(\sqrt{K}t), \tag{3.2}$$

or they can be represented implicitly by the equation $H = \tfrac{1}{2}K^2$, that is,

$$\mathcal{P}^2 - K\mathcal{E}^2 + \tfrac{1}{4}\mathcal{E}^4 = 0. \tag{3.3}$$

C. Stable and unstable manifolds of surviving equilibria

The line $\mathcal{E}=\mathcal{P}=0$ is invariant under the flow of Eqs. (3.1) for $\varepsilon>0$. Equation (3.1c) shows that this line consists of two orbits that contract exponentially towards the equilibrium at $\mathcal{E}=\mathcal{P}=0$, $K=1$. The stability matrix at that equilibrium is

$$\begin{bmatrix} -\varepsilon\alpha & 1 & 0 \\ 1 & -\varepsilon\beta & 0 \\ 0 & 0 & -\varepsilon\gamma \end{bmatrix}$$

and its eigenvalues are

$$\lambda_{1,2} = -\frac{\varepsilon(\alpha+\beta)}{2} \mp \left[\left(\frac{\varepsilon(\alpha-\beta)}{2}\right)^2 + 1\right]^{1/2}, \quad \lambda_3 = -\varepsilon\gamma. \tag{3.4}$$

Thus this equilibrium is a saddle for $\varepsilon^2\alpha\beta<1$ and a sink for $\varepsilon^2\alpha\beta>1$. The corresponding eigenvectors are

$$e_1 = \begin{bmatrix} \dfrac{\varepsilon(\beta-\alpha)}{2} - \left[\left(\dfrac{\varepsilon(\alpha-\beta)}{2}\right)^2 + 1\right]^{1/2} \\ 1 \\ 0 \end{bmatrix},$$

$$e_2 = \begin{bmatrix} 1 \\ \dfrac{\varepsilon(\alpha-\beta)}{2} + \left[\left(\dfrac{\varepsilon(\alpha-\beta)}{2}\right)^2 + 1\right]^{1/2} \\ 0 \end{bmatrix}, \tag{3.5}$$

$$e_3 = \begin{bmatrix} 0 \\ 0 \\ 1 \end{bmatrix}.$$

If ε is close enough to 0, part of the skeleton provided by the unperturbed homoclinic manifolds can be proven to persist in the $\mathcal{E}$-$\mathcal{P}$-K phase space. Namely, any line segment $\mathcal{E}=\mathcal{P}=0$, $K_1\leq K\leq K_2$ with $0<K_1<1<K_2$ possesses two-dimensional stable and unstable manifolds, as shown in Fig. 3. As $\varepsilon\to 0$, these two manifolds collapse smoothly onto pieces of the two homoclinic manifolds.
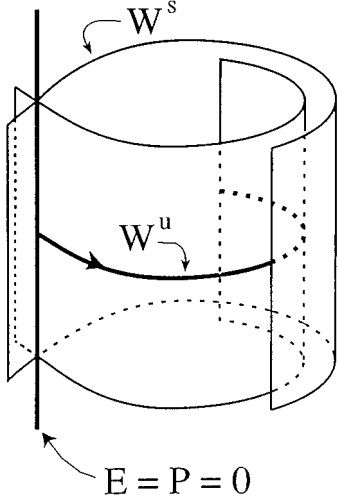
FIG. 3. Geometry of the perturbed stable (W^s) and unstable (W^u) manifolds of the invariant curve $\mathcal{E}=\mathcal{P}=0$ with $K>0$. The stable manifold W^s is also the stable manifold of the saddle at $(\mathcal{E},\mathcal{P},K)=(0,0,1)$. The intersection of the two-dimensional stable manifold W^s with the one-dimensional unstable manifold of the point $(\mathcal{E},\mathcal{P},K)=(0,0,1)$ gives orbits homoclinic to this point.

D. Homoclinic orbits for small ε

Only one pair of homoclinic orbits may survive under perturbation of the whole unperturbed manifold, namely, a pair of orbits homoclinic to the equilibrium at $(\mathcal{E},\mathcal{P},K)=(0,0,1)$. Its survival is determined by the Melnikov method, which is a standard method reviewed, for instance, in [8]. This method shows that the signed distance between the unstable and stable manifolds of the equilibrium at $(0,0,1)$ along the normal to the unperturbed homoclinic manifold

$$\mathbf{n}=\mathbf{\nabla}(H-\tfrac{1}{2}K^2)=(-K\mathcal{E}+\tfrac{1}{2}\mathcal{E}^3,\mathcal{P},-\tfrac{1}{2}\mathcal{E}^2)$$

is proportional to $\varepsilon M(\alpha,\beta,\gamma)+O(\varepsilon^2)$, with a positive proportionality factor. Here

$$M(\alpha,\beta,\gamma)=\int_{-\infty}^{\infty}\langle\mathbf{n},\mathbf{g}\rangle dt \tag{3.6}$$

is the Melnikov function and

$$\mathbf{g}=(-\alpha\mathcal{E},-\beta\mathcal{P},-\alpha\mathcal{E}^2-\gamma(K-\tfrac{1}{2}\mathcal{E}^2-1))$$

is the $O(\varepsilon)$ part of the vector field (3.1). This integral is evaluated along either of the two unperturbed homoclinic orbits (3.2) with $K=1$. Explicitly, the Melnikov function turns out to be

$$M(\alpha,\beta,\gamma)=\tfrac{8}{3}(3\alpha-\beta-2\gamma) \tag{3.7}$$

and so when

$$3\alpha-\beta-2\gamma=0, \tag{3.8}$$

the two branches of the unstable manifold of the equilibrium point $(\mathcal{E},\mathcal{P},K)=(0,0,1)$ return to this point and form a symmetric pair of homoclinic loops.

E. Tracking homoclinic orbits for $\varepsilon=O(1)$

While the Melnikov function shows where the homoclinic orbits survive for $O(\varepsilon)$ relaxation rates, we are interested in where (if anywhere) these homoclinic orbits survive for larger, $O(1)$, relaxation rates. In order to determine this survival, we use the software package AUTO [9] to continue the homoclinic orbits in the parameter space from $O(\varepsilon)$ parameter values to higher values. The homoclinic orbits are approximated by large period (of order 10^3) orbits. Periodic orbits are found through a Hopf bifurcation of the equilibrium points at

$$(\mathcal{E},\mathcal{P},K)=\left[\pm\left(\frac{\gamma}{\alpha}(1-\varepsilon^2\alpha\beta)\right)^{1/2},\pm\varepsilon\sqrt{\alpha\gamma(1-\varepsilon^2\alpha\beta)},\right.$$
$$\left.\times\frac{\gamma}{2\alpha}+\varepsilon^2\left(\alpha\beta-\frac{1}{2}\beta\gamma\right)\right]. \tag{3.9}$$

The Hopf bifurcation occurs along the locus of parameter values given by

$$(\varepsilon\alpha)^2[\varepsilon\alpha+3\varepsilon\beta+\varepsilon\gamma]+\varepsilon\beta+\varepsilon\gamma-\varepsilon\alpha=0. \tag{3.10}$$

The periodic orbits that emanate from these Hopf bifurcations are continued (in ε) to higher period orbits until the period is large enough to approximate the homoclinic orbit. These high period orbits are now continued in the $\varepsilon\alpha$-$\varepsilon\beta$-$\varepsilon\gamma$ parameter space by continuing in $\varepsilon\alpha$-$\varepsilon\beta$ space for fixed values of $\varepsilon\gamma$. The starting point for each fixed $\varepsilon\gamma$ slice is taken for small $\varepsilon\alpha$ and $\varepsilon\beta$ such that the parameters satisfy the Melnikov function's zeros requirement (3.7). The continuation of approximate homoclinic orbits in the parameter space is shown as dotted lines in Fig. 4.

Figure 4 shows the locus of parameter values where homoclinic orbits exist (dotted lines) and the Hopf bifurcation locus (dashed lines) in the $\varepsilon\alpha$-$\varepsilon\beta$ plane for various values of $\varepsilon\gamma$. The orbits exist as predicted by the Melnikov method when ε is small in (3.8). This corresponds to the nearly linear portion of the curve near the origin for each of the dotted curves in Fig. 4. The numerical technique of tracking the homoclinic orbits as ε increases by using AUTO ensures that the same homoclinic orbits that exist at small ε on the lower, nearly linear branch of the dotted curves in Fig. 4 continue to exist at larger ε as we move around the dotted curves to the upper branch in each figure. Figure 4 shows that increasing $\varepsilon\gamma$ decreases the extent of the curve in the parameter space on which the homoclinic orbits exist. Increasing $\varepsilon\gamma$ also decreases the extent of the dashed curve in the $\varepsilon\alpha$-$\varepsilon\beta$ plane in Fig. 4 on which the Hopf bifurcation occurs and thus of the region in which the spiral-sink equilibrium points become spiral-source equilibrium points. For small values of ε there remains a gap of length $\tfrac{2}{3}\varepsilon\beta+\tfrac{1}{3}\varepsilon\gamma+O(\varepsilon^3)$ between the
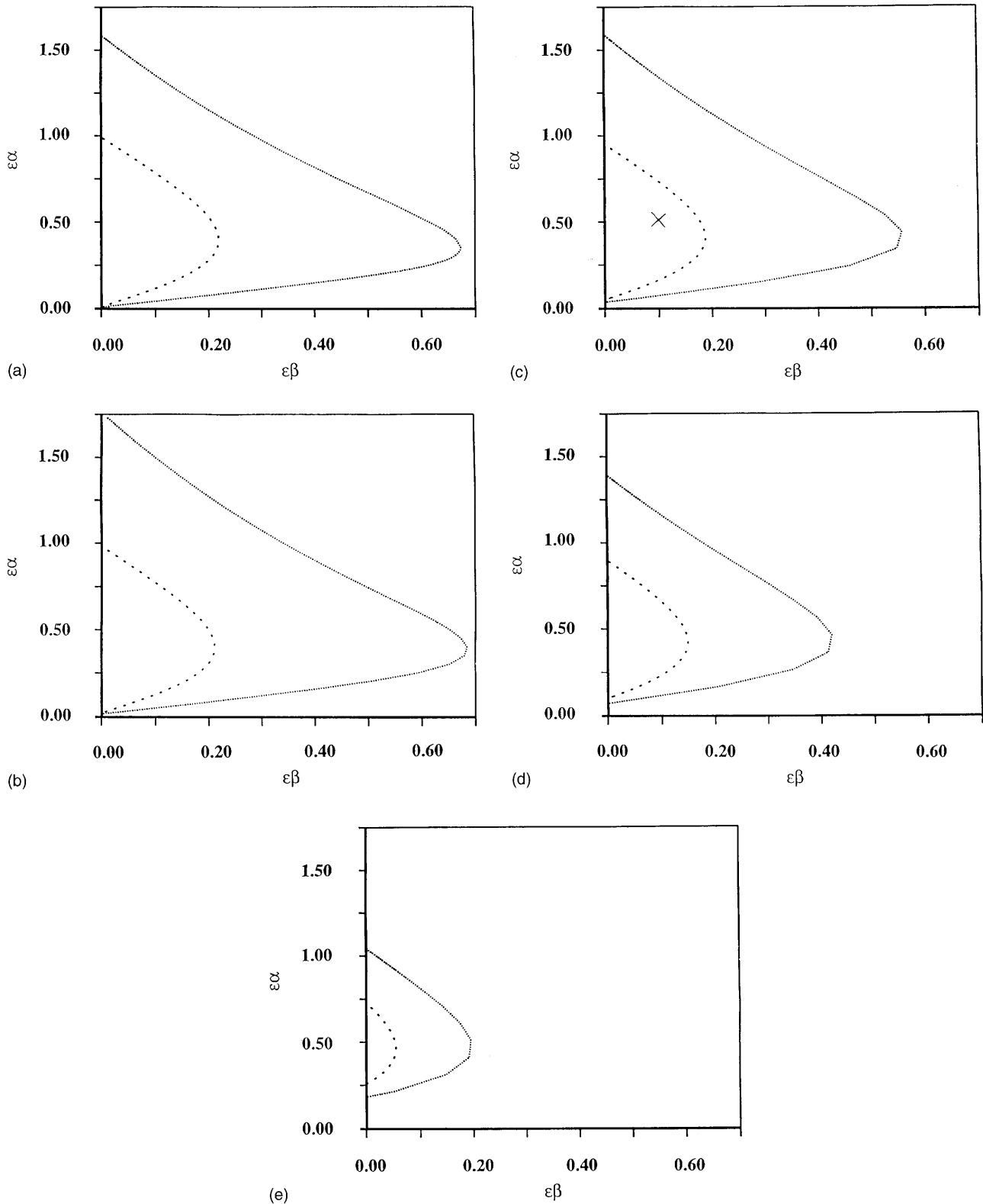
FIG. 4. The dotted line represents the locus of points in the $\varepsilon\alpha$-$\varepsilon\beta$ plane where there exist orbits homoclinic to the completely inverted state $(\mathcal{E},\mathcal{P},\mathcal{K})=(0,0,1)$ of the three-dimensional model at fixed values of $\varepsilon\gamma$: (a) $\varepsilon\gamma=0.01$, (b) $\varepsilon\gamma=0.02$, (c) $\varepsilon\gamma=0.05$, (d) $\varepsilon\gamma=0.1$, and (e) $\varepsilon\gamma=0.226$. The dashed line represents the corresponding curve of Hopf bifurcations given by formula (3.10).

curves defined by Eqs. (3.8) and (3.10) for the existence of homoclinic orbits and the onset of the Hopf bifurcation, respectively.

Outside the dashed curve in Fig. 4, the trajectories tend to spiral-sink equilibrium points, so complex dynamics is not observed outside the dashed curve. However, inside the dashed curve, in the region where these equilibrium points are unstable, complex dynamics (such as chaos) does occur. We will see in the next section that this is the parameter region in which the Lorenz attractor occurs.
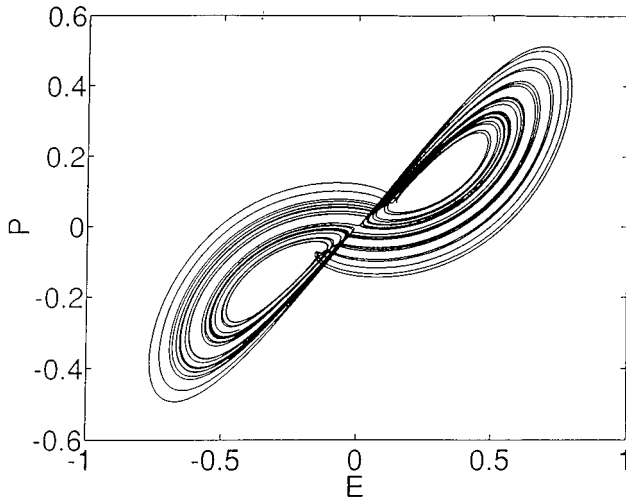
FIG. 5. The strange attractor for the three-dimensional model equations at $(\varepsilon\alpha,\varepsilon\beta,\varepsilon\gamma)=(0.5,0.1,0.05)$ is the usual Lorenz attractor. Its position in the parameter space is the point marked with an $\times$ in Fig. 4(c).

IV. REVIEW OF THE CONNECTION WITH THE LORENZ EQUATIONS AND LASER EXPERIMENTS

A. The Haken transformation

For parameter values near the loci shown as dotted lines in Fig. 4, but in the parameter region where the homoclinic orbits no longer survive, chaotic dynamics may ensue and a strange attractor may form. Computer simulations of the Maxwell-Bloch equations (3.1) show the existence of a strange attractor near the parameter values $(\varepsilon\alpha,\varepsilon\beta,\varepsilon\gamma)=(0.5,0.1,0.05)$. A projection of this strange attractor is shown in Fig. 5. Haken [16] has shown that the real Maxwell-Bloch system (3.1) transforms into the Lorenz equations

$$\frac{dX}{d\tau}=-\sigma X+\sigma Y, \tag{4.1a}$$

$$\frac{dY}{d\tau}=-XZ+\rho X-Y, \tag{4.1b}$$

$$\frac{dZ}{d\tau}=XY-bZ \tag{4.1c}$$

under the change of variables

$$t\to\frac{\sigma}{\varepsilon\alpha}\,\tau, \quad \mathcal{E}\to\frac{\varepsilon\alpha}{\sigma}\,X, \quad \mathcal{P}\to\frac{\varepsilon^2\alpha^2}{\sigma}\,Y,$$

$$\mathcal{D}\to\frac{\varepsilon^2\alpha^2}{\sigma}\,(\rho-Z), \tag{4.2}$$

with new parameters b,σ,ρ defined by

$$\sigma=\frac{\alpha}{\beta}, \quad b=\frac{\gamma}{\beta}, \quad \rho=\frac{1}{\alpha\beta\varepsilon^2}.$$

Hence the attractor that we see in Fig. 5 is in fact the well-known Lorenz attractor, viewed in $\mathcal{E}$-$\mathcal{P}$-$\mathcal{D}$ space.

B. Laser experiments and the Lorenz attractor

Laser experiments by Arecchi [4,17] and by Weiss and co-workers [5,18–23] based on approximations corresponding to system (3.1) have verified the Lorenz attractor description of single-mode laser dynamics in some parameter regimes. Specifically, Arecchi [4] shows that system (3.1) applies in single-mode laser experiments and that the Lorenz attractor is observable when the parameters are all of the same order of magnitude, as we assume. The perturbation parameter ε in system (3.1) corresponds to the inverse of the coupling constant g of the laser equations in Arecchi's mathematical model [4]. Hence the integrable limit we consider as $\varepsilon\to0$ is also the strong-coupling limit, in which $g\to\infty$. Weiss and co-workers [5,18–23] have experimentally observed Lorenz attractor behavior in a single-mode laser near the parameter ratios $\alpha/\beta=4.5$ and $\gamma/\beta=0.25$. For each value of $\varepsilon\gamma$ these two ratios will define a unique point in the $\varepsilon\alpha$-$\varepsilon\beta$ plane. In the case of $\varepsilon\gamma=0.02$, we have $\varepsilon\alpha=0.36$ and $\varepsilon\beta=0.08$, which, not unexpectedly, lies in the region enclosed by the dashed curve in Fig. 4(b).

C. High-Rayleigh-number limit of the Lorenz equations

As we see in (4.2), the $\varepsilon\to0$ limit of Eqs. (3.1) corresponds to the limit of the Lorenz equations as the Rayleigh number ρ goes to infinity. This limit has been studied from various viewpoints in [11,15,24–28]. In particular, Robbins [24], Fowler and McGuiness [25], Fowler [26], and Sparrow [11] analyze periodic orbits in the high-Rayleigh-number limit using the method of averaging and conjecture the existence of a pair of homoclinic orbits. Pokrovskii [15,27] shows the existence of these homoclinic, as well as the existence of adjacent periodic orbits, also by using the method of averaging and Poincaré return map techniques. Li and Zhang [28] find formula (3.8) for the existence of homoclinic orbits in this limit by the Melnikov method and also address perturbations of periodic orbits of the infinite-Rayleigh-number case by using the subharmonic Melnikov method. The results in Fig. 4 for the Maxwell-Bloch system (3.1) when translated to the Lorenz system (4.1) by the change of variables in (4.2) show that the homoclinic orbits that exist in the infinite-Rayleigh-number limit also persist for $O(1)$ values of ρ.

D. Shooting approaches to the homoclinic orbits

Computations by Kaplan and Yorke [10] have shown the existence of a homoclinic orbit in the Lorenz equations at the particular set of parameter values $(b,\sigma,\rho)=(\frac{8}{3},10,13.926)$, which is equivalent to $(\varepsilon\alpha,\varepsilon\beta,\varepsilon\gamma)=(0.847,0.085,0.226)$ for the Maxwell-Bloch equations. This value lies on the upper branch of the locus of parameter values where homoclinic orbits exist in Fig. 4(e). A similar result on the existence of this homoclinic orbit has been shown by Sparrow [11].

Recently, Hastings and Troy [29,30] and Hassard and Zhang [31] have given rigorous proofs of the existence of these homoclinic orbits by shooting methods using precise computer arithmetic. These homoclinic orbits are also found

on the upper branch of the parameter curves in Fig. 4. We show that the upper and lower branches of the locus of parameter values at which homoclinic orbits exist are continuously connected to each other. Therefore, the homoclinic orbits that have been previously found by shooting methods in the Lorenz system are in fact the same homoclinic orbits that we have found to exist analytically in the integrable limit of the Maxwell-Bloch equations.

V. CHAOTIC DYNAMICS

A. Poincaré return map

In order to explain the manifestation of the chaotic dynamics, we follow [8,10,32] in constructing a Poincaré return map in the vicinity of the pair of homoclinic loops and showing that as the loops break, this map becomes a Smale horseshoe map. Since this construction is by now standard, we only describe its properties that pertain specifically to our problem. In particular, the construction contains several hypotheses that must be checked on a case-by-case basis. In our problem, they can in fact be checked analytically and we briefly describe how this can be done.

B. Local coordinates

We examine the dynamics by first fixing $\varepsilon\alpha$, $\varepsilon\beta$, and $\varepsilon\gamma$ such that a pair of homoclinic orbits exists. Equations (3.1) are transformed from the $\mathcal{E}$-$\mathcal{P}$-K coordinates into u-v-z coordinates in the eigendirections (3.5) so that the point $(\mathcal{E},\mathcal{P},K)=(0,0,1)$ is translated to the origin and the coordinate axes become aligned with the eigenvectors (3.5) of the linearization of Eqs. (3.1) about the origin. The unstable manifold of the origin is tangent to the v axis and the stable manifold is tangent to the u-z plane. The two homoclinic loops return to the origin tangent to the z axis. Moreover, the symmetry of the system under the transformation $(u,v,z) \mapsto (-u,-v,z)$ (which is inherited from the $\mathcal{E}$-$\mathcal{P}$-K coordinates) forces both homoclinic loops to return to the origin with the same sign of z. We can choose the z axis so that this coordinate is positive. Recalling the eigenvalues of the linearized system (3.4), we see that $\lambda_1,\lambda_3<0$ and $\lambda_2>0$ and also that $|\lambda_1|>|\lambda_2|$. We further assume that $|\lambda_2|>|\lambda_3|$ so that we have a strongly contracting direction along u and a strongly expanding direction along v. This assumption is satisfied if and only if $\varepsilon^2\gamma(\alpha+\beta+\gamma)<1$, which occurs for small dissipation ($\varepsilon\ll1$).

C. Transverse cross sections to the flow in local coordinates

We can now show that system (3.1) exhibits chaotic dynamics. We begin by constructing a square box of size 2Δ centered at the origin, shown in Fig. 6. The pair of homoclinic orbits exits this box through the sides at $v=\pm\Delta$ and return to it through the top at $z=\Delta$, which we denote by Π. The stable manifold of the origin intersects the top of the box Π along a curve $v=V(u)$. For small Δ, this curve is $O(\Delta^2)$ close to the line $v=0$. If we denote by Π^+ and Π^- the portions of the top of the box Π with $v>V(u)$ and $v<V(u)$, respectively, then we can define the Poincaré map P as the map that takes the points on Π^+ and Π^- and evolves them in time until they return to the plane $z=\Delta$.
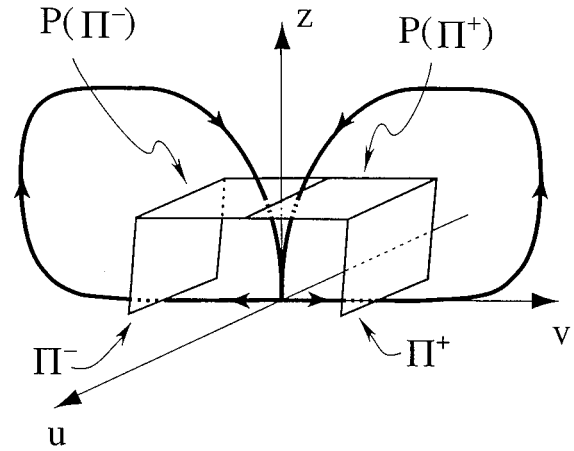

FIG. 6. Cross sections to the unperturbed homoclinic orbits used in the construction of the Poincaré map.

Clearly, points on Π^+ follow the homoclinic loop with $v>0$ and points on Π^- follow the homoclinic loop with $v<0$.

D. Construction of the return map

Linear local analysis near the origin shows that the images of the surfaces Π^+ and Π^- on the sides of the box are wedge shaped and the flow near the two homoclinic loops returns the two wedges to the plane $z=\Delta$ in one of the two ways depicted in Fig. 7. In particular, the image $P(\Pi^\pm)$ can intersect either $\Pi^\pm$ or $\Pi^\mp$ (but not both), which depends on
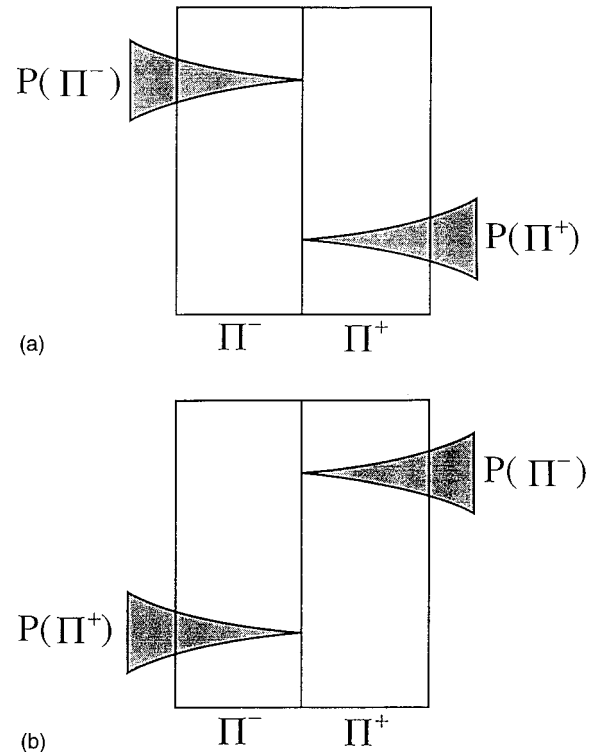

FIG. 7. Geometry of the images $P(\Pi^\pm)$ of the surfaces $\Pi^\pm$ under the Poincaré map (a) for homoclinic orbits with no twist and (b) for homoclinic orbits with a $180°$ twist. The wedge shape of the images is found from linear analysis of Eqs. (3.1) near the origin.
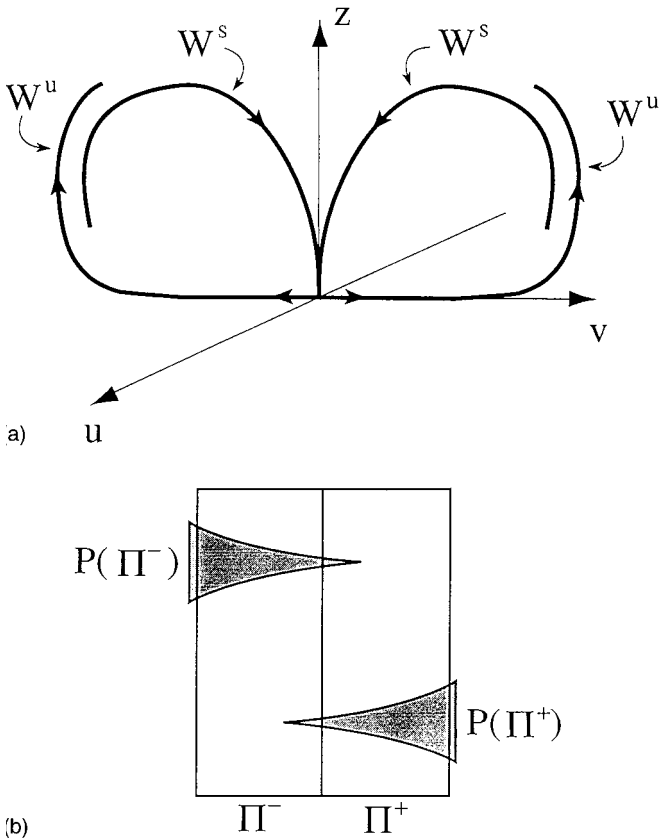
FIG. 8. Geometry of the perturbed system near the homoclinic orbits at $\varepsilon\alpha=(\varepsilon\alpha)_{\text{crit}}$: (a) the breaking of the homoclinic loops and (b) the images $P(\Pi^{\pm})$ of the surfaces $\Pi^{\pm}$.

whether the stable manifold of the origin has a 180° twist along the homoclinic loops as they travel from the sides of the box to its top. In our case, when $\varepsilon \ll 1$, the geometry of the nearby unperturbed system shows that no such twist is possible, so that the image $P(\Pi^{\pm})$ only intersects $\Pi^{\pm}$. This is in contrast with the upper branch of the $\varepsilon\alpha$-$\varepsilon\beta$-$\varepsilon\gamma$ surface of homoclinic orbits, where Kaplan and Yorke [10] have numerically observed the 180° twist.

We now fix small $\varepsilon\beta$ and $\varepsilon\gamma$ and increase $\varepsilon\alpha$ through $(\varepsilon\alpha)_{\text{crit}}$, for which the pair of homoclinic orbits exists, given by the zeros of (3.7). Simultaneously, the two homoclinic loops will break in the way depicted in Fig. 8(a), which implies that the images of the surfaces Π^{+} and Π^{-} move in the way depicted in Fig. 8(b). This fact is shown in the following way. Recall that the signed distance between the one-dimensional unstable manifold and the two-dimensional stable manifold of the point $(\mathcal{E},\mathcal{P},K)=(0,0,1)$ in the direction of the outward pointing normal on the unperturbed homoclinic manifold is proportional to $\varepsilon M(\alpha,\beta,\gamma)+O(\varepsilon^{2})$ with a positive proportionality factor. Now for $\varepsilon\alpha>(\varepsilon\alpha)_{\text{crit}}$, we have $M(\alpha,\beta,\gamma)=\frac{8}{3}(3\alpha-\beta-2\gamma)>0$ so that the unstable manifold is outside the stable manifold. Similarly, the unstable manifold is inside the stable manifold in the case when $\varepsilon\alpha<(\varepsilon\alpha)_{\text{crit}}$. As a consequence, for $\varepsilon\alpha>(\varepsilon\alpha)_{\text{crit}}$ the images $P(\Pi^{\pm})$ penetrate into $\Pi^{\pm}$, while for $\varepsilon\alpha<(\varepsilon\alpha)_{\text{crit}}$ they only intersect $\Pi^{\pm}$. As shown in [10,32] and reviewed in [8], P thus becomes a Smale horseshoe map for $\varepsilon\alpha>(\varepsilon\alpha)_{\text{crit}}$. This confirms the expectations that the chaotic dynamics is

present inside the region in the $\varepsilon\alpha$-$\varepsilon\beta$-$\varepsilon\gamma$ space enclosed by the two-dimensional locus of parameter values where homoclinic loops exist.

E. Observable chaotic dynamics

The chaotic dynamics associated with these homoclinic orbits is robust with respect to small parameter deviations so chaos exists in a parameter region somewhere inside of the dotted curve in Fig. 4. However, the spiral-sink equilibrium points (3.9) are stable for the parameter values at which these homoclinic orbits exist. Therefore, most trajectories will not notice the homoclinic chaos since they will tend to one of these stable equilibrium points. When parameter values are further changed, the equilibrium points may become unstable and the long-term dynamics would then either lie on a strange attractor or follow a stable limit cycle (if one exists). Recall that these equilibria are unstable in the parameter regions enclosed by the dashed lines in Fig. 4. For instance, the parameter values for the chaotic trajectory shown in Fig. 5 do lie within one of these regions, as shown by $\times$ in Fig. 4(c). The chaotic dynamics is manifested as random switching of phase points between orbits that follow the surviving homoclinic orbits.

Figure 9 shows a sequence of two-dimensional $\mathcal{E}$-$\mathcal{P}$ projections of phase trajectories for the Maxwell-Bloch system (3.1) as the parameter $\varepsilon\alpha$ increases at constant $\varepsilon\beta$ and $\varepsilon\gamma$, along a vertical line in the $\varepsilon\alpha$-$\varepsilon\beta$ plane. The initial phase point is the same in each case. For $\varepsilon\alpha$ small and below the dotted line in Fig. 4(a), Fig. 9(a) shows that the solution approaches a spiral-sink equilibrium. As $\varepsilon\alpha$ increases to match the homoclinic orbit condition (3.8), the solution behavior shows little change; see Fig. 9(b). At higher values of $\varepsilon\alpha$ the trajectory approaches a limit cycle; see Fig. 9(c). Figure 9(d) shows that this limit cycle persists as $\varepsilon\alpha$ increases up to the Hopf bifurcation value of condition (3.10), the dashed curve in Fig. 4(a). Finally, as $\varepsilon\alpha$ increases further, the solution tends to the Lorenz attractor whose $\mathcal{E}$-$\mathcal{P}$ projection is shown in Fig. 9(e). We expect that this bifurcation sequence would be observable in single-mode laser experiments, although as far as we know it has not yet been seen.

The small separation of parameters in the region of this bifurcation sequence suggests that the breakup of homoclinic orbits plays a significant role in the formation of the attractor itself. This has been conjectured before [10,11] in different parameter regimes (the upper branch in Fig. 4). However, it seems plausible that near the lower branch the homoclinic orbit breakup would be effective, since the separation in parameters between regular and chaotic behavior is smaller.

VI. THE CASE WITH THE PROBE

A. Five-dimensional dynamics

When the dynamics of the Maxwell-Bloch equations with a weak probe is considered, we return to the full five-dimensional equations (1.2). The addition of the probe laser breaks the circular symmetry that was present in the case with no probe. Again, we eliminate the inversion $\mathcal{D}$ in favor of the energy K in Eqs. (1.2) to yield the five-dimensional system (recalling that the electric field envelope $\mathcal{E}$ and the polarizability envelope $\mathcal{P}$ are complex)
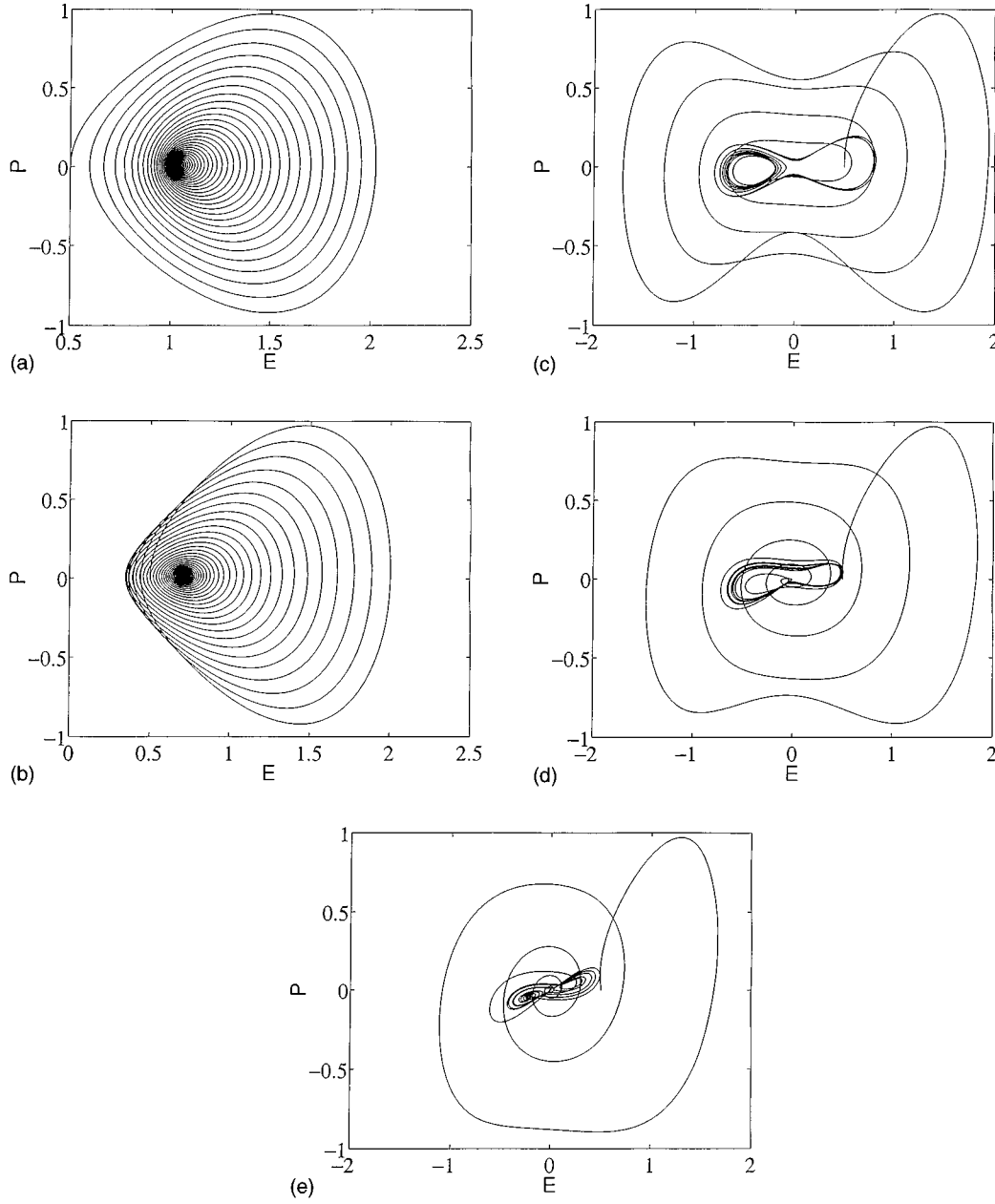
FIG. 9. Bifurcation sequence as $\varepsilon\alpha$ increases for fixed $\varepsilon\beta=0.04$ and $\varepsilon\gamma=0.01$ in the three-dimensional model. The trajectories are two-dimensional projections of the true trajectories: (a) $\varepsilon\alpha=0.01$, (b) $\varepsilon\alpha=0.02$, (c) $\varepsilon\alpha=0.05$, (d) $\varepsilon\alpha=0.1$, and (e) $\varepsilon\alpha=0.2$.

$$\dot{\mathcal{E}}=\mathcal{P}-\varepsilon\alpha\mathcal{E}, \tag{6.1a}$$

$$\dot{\mathcal{P}}=(\mathcal{E}+\varepsilon\delta e^{i\omega t})(K-\tfrac{1}{2}|\mathcal{E}|^2)-\varepsilon\beta P, \tag{6.1b}$$

$$\dot{K}=-\tfrac{1}{2}\varepsilon\delta(e^{i\omega t}\mathcal{P}^*+e^{-i\omega t}\mathcal{P})-\varepsilon\alpha|\mathcal{E}|^2$$
$$-\varepsilon\gamma(K-\tfrac{1}{2}|\mathcal{E}|^2-1). \tag{6.1c}$$

This system is a nonautonomous perturbation of the integrable case (2.5).

When $\varepsilon=0$, the $\mathcal{E}$-$\mathcal{P}$ dynamics is governed by a family of complex Duffing oscillators (2.5) parametrized by K. In the full $\mathcal{E}$-$\mathcal{P}$-K phase space, the curve of completely inverted state equilibria at $\mathcal{E}=\mathcal{P}=0$, $K>0$ is connected to itself by a family of two-dimensional homoclinic tori given by (2.7). We recall that these homoclinic tori are represented implicitly by Eqs. (2.8).

B. Rotating coordinate frame

To study the perturbed situation, we rewrite the Maxwell-Bloch equations in an autonomous form by transforming the system (6.1) to a rotating frame, letting $x=\mathcal{E}e^{-i\omega t}$ and $y=\mathcal{P}e^{-i\omega t}$ to yield

$$\dot{x}_1=\omega x_2+y_1-\varepsilon\alpha x_1, \tag{6.2a}$$

$$\dot{x}_2=-\omega x_1+y_2-\varepsilon\alpha x_2, \tag{6.2b}$$

$$\dot{y}_1=\omega y_2+(x_1+\varepsilon\delta)(K-\tfrac{1}{2}|x|^2)-\varepsilon\beta y_1, \tag{6.2c}$$

$$\dot{y}_2 = -\omega y_1 + x_2(K - \tfrac{1}{2}|x|^2) - \varepsilon\beta y_2, \qquad (6.2d)$$

$$\dot{K} = -\varepsilon\delta y_1 - \varepsilon\alpha|x|^2 - \varepsilon\gamma(K - \tfrac{1}{2}|x|^2 - 1), \qquad (6.2e)$$

where x_1 and x_2 are the real and imaginary parts of x, respectively, and similarly for y. We apply the same transformation to the homoclinic solution of the unperturbed problem. In this rotating frame, the homoclinic solutions for the unperturbed problem are represented as

$$x = 2\sqrt{K} \; \mathrm{sech}(\sqrt{K}t) e^{i(\theta - \omega t)},$$

$$\qquad\qquad\qquad\qquad\qquad\qquad (6.3)$$

$$y = -2K \; \mathrm{sech}(\sqrt{K}t)\tanh(\sqrt{K}t) e^{i(\theta - \omega t)}.$$

C. A perturbed spiral-saddle equilibrium and its stable and unstable manifolds

While the curve $\mathcal{E} = \mathcal{P} = 0$ is no longer invariant under the perturbation, there is a nearby curve that is invariant for ε close enough to zero and, furthermore, along this invariant curve the orbits contract towards an equilibrium point that is $O(\varepsilon^2)$ close to the point $(x,y,K) = (0,0,1)$. In other words, the skeleton provided by the homoclinic manifolds of the unperturbed problem still persists under small perturbation, but in a slightly altered form. The invariant curve will still possess stable and unstable manifolds that will collapse smoothly onto part of the unperturbed homoclinic manifold as $\varepsilon \to 0$. Orbits for which these perturbed manifolds intersect will be the surviving homoclinic orbits under the perturbation.

D. Homoclinic orbits persisting for small ε

The surviving homoclinic orbits are again computed by the Melnikov method. However, we now use a two-component Melnikov vector in order to compute the distance between the stable and unstable manifolds of the spiral saddle near $(x,y,K) = (0,0,1)$, rather than the scalar Melnikov function used in the case with no probe. The corresponding distance between these stable and unstable manifolds will be zero only when both components of the Melnikov vector have simultaneous simple zeros.

The two components of the Melnikov vector $\mathbf{M} = (M_1, M_2)^T$ are given by

$$M_1(\alpha,\beta,\gamma,\delta,\omega,\theta) = \int_{-\infty}^{\infty} \langle \mathbf{n}_1, \mathbf{g} \rangle dt, \qquad (6.4a)$$

$$M_2(\alpha,\beta,\gamma,\delta,\omega,\theta) = \int_{-\infty}^{\infty} \langle \mathbf{n}_2, \mathbf{g} \rangle dt, \qquad (6.4b)$$

where

$$\mathbf{n}_1 = \boldsymbol{\nabla}(H - \tfrac{1}{2}K^2) = (-Kx_1 + \tfrac{1}{2}x_1^3 + \tfrac{1}{2}x_1x_2^2, -Kx_2 + \tfrac{1}{2}x_2^3 + \tfrac{1}{2}x_1^2$$

$$+ x_2, y_1, y_2, -\tfrac{1}{2}|x|^2),$$

$$\mathbf{n}_2 = \boldsymbol{\nabla}(J) = (-y_2, y_1, x_2, -x_1, 0)$$

are the two normals to the unperturbed homoclinic manifold (2.8) and the vector

$$\mathbf{g} = (-\alpha x_1, -\alpha x_2, \delta(K - \tfrac{1}{2}|x|^2) - \beta y_1, -\beta y_2, -\delta y_1 - \alpha|x|^2$$

$$-\gamma(K - \tfrac{1}{2}|x|^2 - 1))$$

is the $O(\varepsilon)$ part of the vector field of the equations in the rotating frame (6.2). The Melnikov vector is evaluated along the unperturbed homoclinic orbits (6.3). We evaluate the Melnikov vector at $K = 1$, which we know to be $O(\varepsilon^2)$ close to the K coordinate of the equilibrium point. The Melnikov vector is explicitly given by

$$M_1(\alpha,\beta,\gamma,\delta,\omega,\theta) = \frac{8}{3}(3\alpha - \beta - 2\gamma)$$

$$+ \frac{2}{3}\pi\delta\omega(\omega^2 - 2)\mathrm{sech}\left(\frac{\pi\omega}{2}\right)\sin(\theta), \qquad (6.5a)$$

$$M_2(\alpha,\beta,\gamma,\delta,\omega,\theta) = -2\pi\delta\omega^2 \sin(\theta)\mathrm{sech}\left(\frac{\pi\omega}{2}\right). \qquad (6.5b)$$

The two components of the Melnikov vector simultaneously have simple zeros at the values

$$3\alpha - \beta - 2\gamma = 0, \quad \theta = 0 \text{ or } \pi. \qquad (6.6)$$

Hence homoclinic orbits will exist (for small ε) when (α,β,γ) satisfy the relationship (6.6).
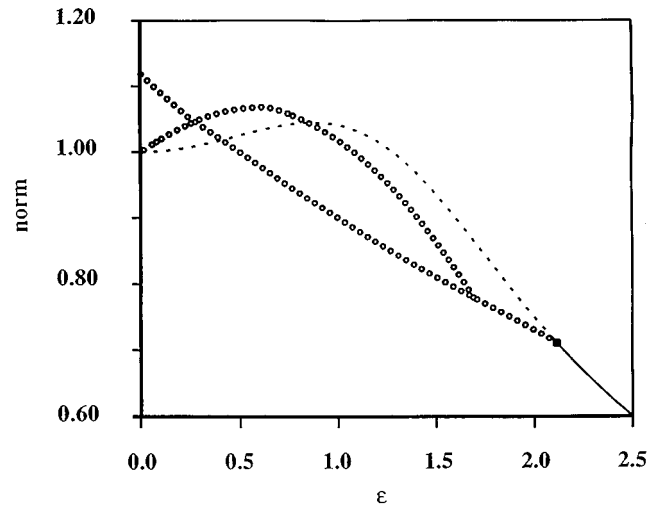

FIG. 10. Bifurcation structure for finding the approximate homoclinic orbit in the five-dimensional model with $(\alpha,\beta,\gamma) = (0.1,0.1,0.1)$. The equilibrium at $(\mathcal{E},\mathcal{P},K) = (0,0,1)$ undergoes a Hopf bifurcation near $\varepsilon = 2.1$. The periodic orbits that emanate from this bifurcation approach the homoclinic orbit as $\varepsilon \to 0$.
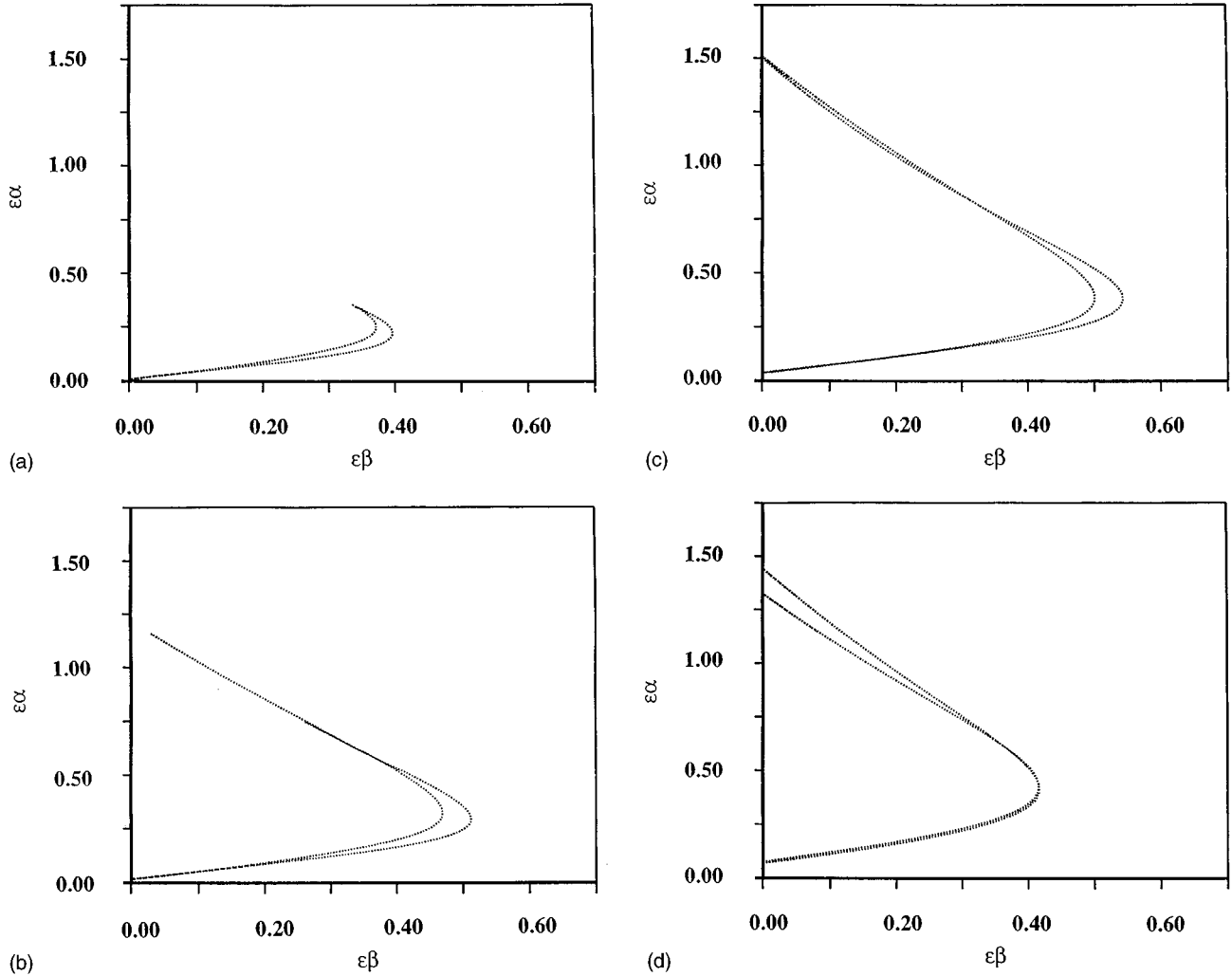
FIG. 11. Locus of points in the $\varepsilon\alpha$-$\varepsilon\beta$ plane where there exist orbits homoclinic to the completely inverted state at $(\mathcal{E},\mathcal{P},K)=(0,0,1)$ of the five-dimensional model at the pumping amplitude $\varepsilon\delta=0.1$ and fixed values of $\varepsilon\gamma$: (a) $\varepsilon\gamma=0.01$, (b) $\varepsilon\gamma=0.02$, (c) $\varepsilon\gamma=0.05$, and (d) $\varepsilon\gamma=0.1$.

E. Comparison with probeless case

The circular symmetry of equations (1.1) with no probe causes an entire circle of homoclinic orbits to exist under perturbation (when the Melnikov function has transverse zeros); however, in Eqs. (1.2) with nonzero δ, this symmetry has been broken and only one homoclinic orbit from the entire circle will persist. In fact, since the Melnikov function has transverse zeros for both $\theta=0$ and π, two homoclinic orbits will persist, one for each of these two values. However, the Melnikov function only gives an $O(\varepsilon)$ result, so these two homoclinic orbits may exist at parameter values that are $O(\varepsilon^2)$ away from each other.

F. Tracking homoclinic orbits $\varepsilon=O(1)$

As in the case with no probe, we are interested in the survival, at larger relaxation rates, of the homoclinic orbits that we computed for small ε by the Melnikov method. Again we use the software package AUTO [9] to continue approximate homoclinic orbits in the parameter space from $O(\varepsilon)$ relaxation rates to higher values. However, in the case with the probe ($\delta\neq0$), the only equilibrium point is the one that is near $(x,y,K)=(0,0,1)$ for small ε, so we can only

trace periodic orbits that emanate from a Hopf bifurcation of this equilibrium point. The bifurcation diagram for this equilibrium point is shown in Fig. 10. Periodic orbits that are created from the Hopf bifurcation split into two branches: one that becomes the homoclinic orbit as $\varepsilon\to0$ and one that heads toward orbits of period $2\pi/\omega$ as $\varepsilon\to0$. The orbits of period $2\pi/\omega$ correspond to the equilibrium points in the $\mathcal{E}$-$\mathcal{P}$-$\mathcal{D}$ frame (periodic orbits in the rotating frame) at

$$|x|^2=2(\omega^2+K), \quad y=i\omega x,$$

which exist in the limit as $\varepsilon\to0$.

The approximate homoclinic orbits are continued in the $\varepsilon\alpha$-$\varepsilon\beta$-$\varepsilon\gamma$ parameter space for fixed $\varepsilon\delta$ and ω. The starting point for each fixed $\varepsilon\gamma$ slice is taken for small $\varepsilon\alpha$ and $\varepsilon\beta$ such that the linear relationship (6.6) is satisfied. The continuation of these orbits in $\varepsilon\alpha$-$\varepsilon\beta$ space for various values of $\varepsilon\gamma$ is shown in Fig. 11. When $\varepsilon\delta$ is relatively small (same order of magnitude as $\varepsilon\gamma$) the homoclinic orbits exist at nearly the same locations of $\varepsilon\alpha$-$\varepsilon\beta$-$\varepsilon\gamma$ parameter space as when there was no probe; see Figs. 12(a) and 12(b). As the probe strength is increased, the homoclinic orbits only exist for small $\varepsilon\alpha$ and $\varepsilon\beta$ parameter values. The combination of a
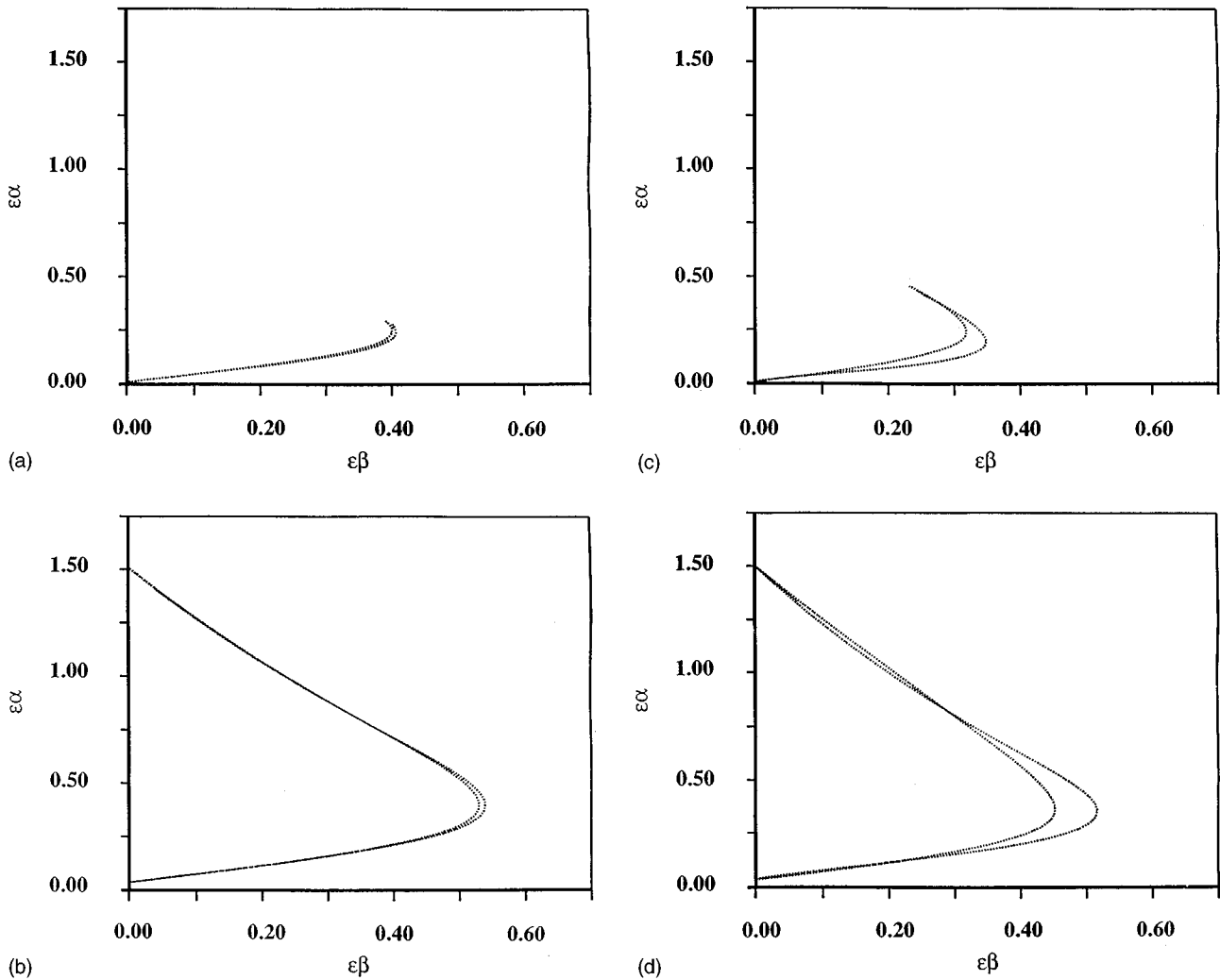
FIG. 12. Locus of points in the $\varepsilon\alpha$-$\varepsilon\beta$ plane where there exist orbits homoclinic to the completely inverted state of the five-dimensional model at various values of the pumping amplitude $\varepsilon\delta$ and fixed values of $\varepsilon\gamma$: (a) $\varepsilon\delta$=0.02, $\varepsilon\gamma$=0.01; (b) $\varepsilon\delta$=0.02, $\varepsilon\gamma$=0.05; (c) $\varepsilon\delta$=0.2, $\varepsilon\gamma$=0.01; and (d) $\varepsilon\delta$=0.2, $\varepsilon\gamma$=0.05.

large probe laser and large relaxation causes the homoclinic orbits to no longer exist; see Figs. 12(c) and 12(d).

As in the case with no probe, the homoclinic orbits exist near the locations in parameter space that the Melnikov function predicted for $O(\varepsilon)$ relaxation rates, as shown by the linear part of the curves in Figs. 11 and 12. As the parameter values are increased, the two curves that were tangent to each other when ε was small can now be distinguished from one another; one corresponds to the θ=0 branch and the other corresponds to the θ=π branch. As the parameter values are further increased, these two branches will become tangent to each other once again. Equations (6.1) will exhibit chaotic dynamics for parameter values that lie inside of these curves. However, as was discussed in the case where there is no probe, the chaos will be unobservable for parameter values very close to the parameter values where homoclinic orbits occur. When $\varepsilon\delta$ is sufficiently small, strange attractors can still be observed for values of the parameters $\varepsilon\alpha$, $\varepsilon\beta$, and $\varepsilon\gamma$ near those obtained in the case with no probe. A sample trajectory in the five-dimensional attractor is shown in Fig. 13.

In this case the chaotic dynamics manifests itself in much the same way as for the case with no probe, that is, as a

random switching of phase points between orbits that follow the two surviving homoclinic orbits. The construction of the Smale horseshoe for this system proceeds in a manner similar to the analogous construction in the three-dimensional case, but its details are somewhat different due to the spiral-saddle nature of the underlying equilibrium point and its ho-
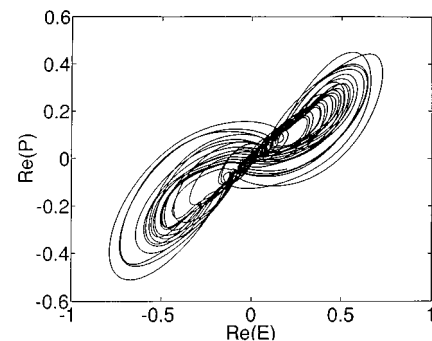

FIG. 13. Two-dimensional projection of a trajectory for the five-dimensional model equations in the chaotic region at $(\varepsilon\alpha,\varepsilon\beta,\varepsilon\gamma,\varepsilon\delta)$ =(0.5,0.1,0.05,0.1). The strange attractor is a perturbation of the complex Lorenz attractor.
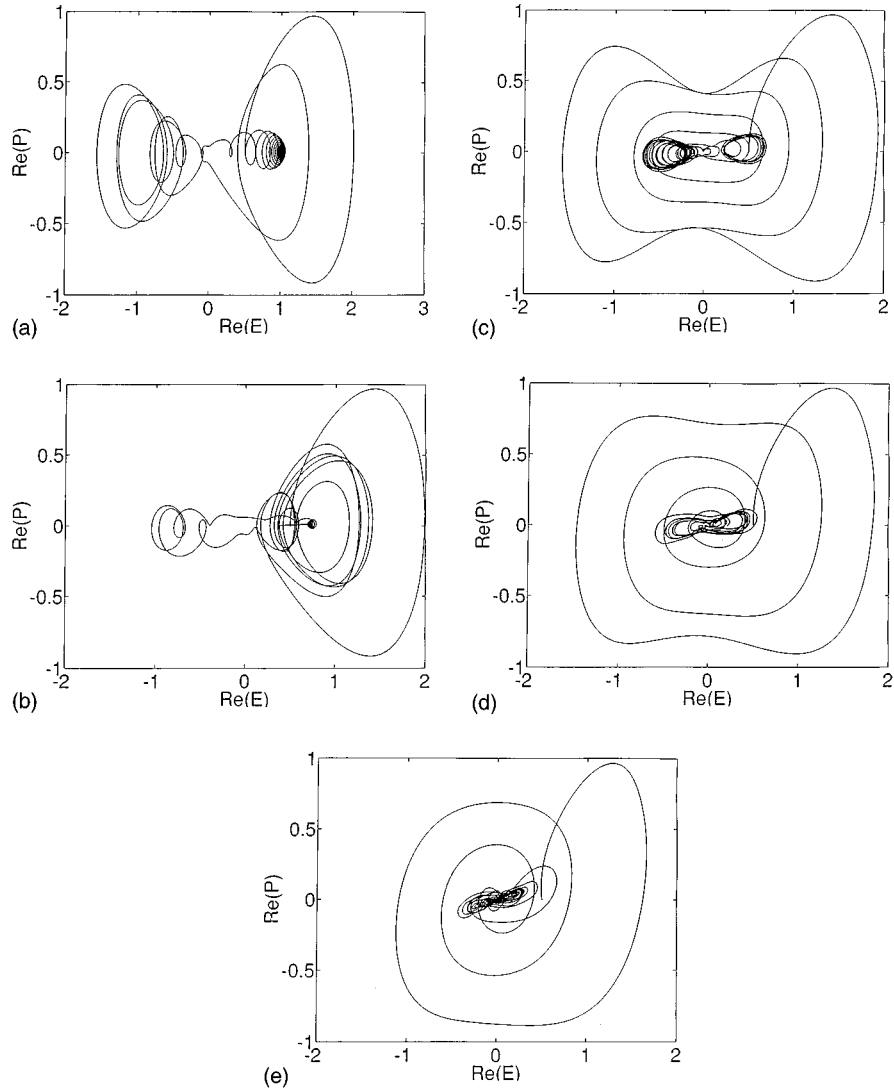
FIG. 14. Bifurcation sequence as $\varepsilon\alpha$ increases for fixed $\varepsilon\beta=0.04$, $\varepsilon\gamma=0.01$, and $\varepsilon\delta=0.1$ in the five-dimensional model. The trajectories are two-dimensional projections of the true trajectories: (a) $\varepsilon\alpha=0.01$, (b) $\varepsilon\alpha=0.02$, (c) $\varepsilon\alpha=0.05$, (d) $\varepsilon\alpha=0.1$, and (e) $\varepsilon\alpha=0.2$.

moclinic orbits. These five-dimensional homoclinic orbits are Šilnikov orbits. The Smale horseshoe construction near these orbits is given in [33–36].

Figure 14 shows a sequence of two-dimensional projections of the five-dimensional phase trajectories for the Maxwell-Bloch system (6.1) as the parameter $\varepsilon\alpha$ increases at constant $\varepsilon\beta$, $\varepsilon\gamma$, and $\varepsilon\delta$ along a vertical line in the $\varepsilon\alpha$-$\varepsilon\beta$ plane. The initial phase point is the same in each case. The bifurcation sequence is similar to the three-dimensional case shown in Fig. 9.

VII. CONCLUSION

We have shown that the Maxwell-Bloch equations with no probe and no dissipation terms possess orbits that are homoclinic to the completely inverted state. With no probe laser, these homoclinic orbits survive perturbation for certain values of dissipation parameters, which were obtained through a combination of the Melnikov technique and numerical continuation. When these orbits break for nearby parameter values, chaos will ensue; however, there still exist stable equilibrium points that attract the trajectories from a given initial condition. The chaotic dynamics becomes observable when these equilibrium points become unstable, and a strange attractor is formed. The connection between the Maxwell-Bloch equations and the singular limit of the Lorenz equations for large Rayleigh number shows that this attractor is the usual Lorenz attractor. When the effects of the probe laser are also included in the model, the homoclinic orbits exist in the same region of the parameter space for small dissipation. However, as the dissipation is increased, the location of homoclinic orbits (in the parameter space) differs greatly from the case with no probe laser. The breaking of these homoclinic orbits for nearby parameter values again causes chaotic dynamics, eventually leading to a strange attractor.

The chaotic dynamics manifests itself as a random switching of orbits that are very close to each of the surviving homoclinic orbits. This phenomenon may be observed as a random "flickering" of the laser light. The homoclinic orbits that have been studied in this paper may be observed in physical situations by using a nonlinear control technique combined with the recent advances in controlling chaotic

systems [37–41]. In particular, this approach is planned to be presented in [42].

ACKNOWLEDGMENTS

[1] L. Allen and J. H. Eberly, *Optical Resonance and Two-Level Atoms* (Dover, New York, 1987).

[2] J. Opt. Soc. B **5** (5) (1988), special issue on nonlinear dynamics of lasers.

[3] J. V. Moloney and A. C. Newell, Physica D **44**, 1 (1990).

[4] F. T. Arecchi, Phys. Scr. **T23**, 160 (1988).

[5] C. O. Weiss, Opt. Quantum Electron. **20**, 1 (1988).

[6] K. N. Alekseev and G. P. Berman, Zh. Éksp. Teor. Fiz. **92**, 1985 (1987) [Sov. Phys. JETP **65**, 1115 (1987)].

[7] D. D. Holm and Gregor Kovačič, Physica D **56**, 270 (1992).

[8] S. Wiggins, *Global Bifurcations and Chaos: Analytical Methods* (Springer-Verlag, New York, 1988).

[9] E. J. Doedel and P. Kernévez, California Institute of Technology Report, 1986 (unpublished).

[10] J. L. Kaplan and J. A. Yorke, Commun. Math. Phys. **67**, 93 (1979).

[11] C. Sparrow, *The Lorenz Equations* (Springer-Verlag, New York, 1982).

[12] E. T. Jaynes and F. N. Cummings, Proc. IEEE **51**, 89 (1963).

[13] D. D. Holm, G. Kovačič, and T. A. Wettergren, Phys. Lett. A **200**, 299 (1995).

[14] D. D. Holm, G. Kovačič, and B. Sundaram, Phys. Lett. A **154**, 346 (1991).

[15] L. A. Pokrovskii, Theor. Math. Phys. **62**, 183 (1986).

[16] H. Haken, Phys. Lett. **53A**, 77 (1975).

[17] F. T. Arecchi, Acta Phys. Austr. **56**, 57 (1984).

[18] C. O. Weiss and W. Klische, Opt. Commun. **51**, 47 (1984).

[19] C. O. Weiss, J. Opt. Soc. Am. B **2**, 137 (1985).

[20] C. O. Weiss, W. Klische, P. S. Ering, and M. Cooper, Opt. Commun. **52**, 405 (1985).

[21] C. O. Weiss, N. B. Abraham, and U. Hübner, Phys. Rev. Lett. **61**, 1587 (1988).

[22] C. O. Weiss, W. Klische, N. B. Abraham, and U. Hübner, Appl. Phys. B **49**, 211 (1989).

[23] M. Y. Li, T. Win, C. O. Weiss, and N. R. Heckenberg, Opt. Commun. **80**, 119 (1990).

[24] K. Robbins, SIAM J. Appl. Math. **36**, 457 (1979).

[25] A. C. Fowler and M. J. McGuinness, Physica D **5**, 149 (1982).

[26] A. C. Fowler, Stud. Appl. Math. **70**, 215 (1984).

[27] L. A. Pokrovskii, Theor. Math. Phys. **67**, 490 (1986).

[28] J. B. Li and J. M. Zhang, SIAM J. Appl. Math. **53**, 1059 (1993).

[29] S. P. Hastings and W. C. Troy, Bull. Am. Math. Soc. **27**, 298 (1992).

[30] S. P. Hastings and W. C. Troy, J. Diff. Equations (to be published).

[31] B. D. Hassard and J. Zhang, SIAM J. Math. Anal. **25**, 179 (1994).

[32] V. S. Afraimovich, V. V. Bykov, and L. P. Šilnikov, Trans. Moscow Math. Soc. **2**, 153 (1983).

[33] L. P. Šilnikov, Sov. Math. Dokl. **6**, 163 (1965).

[34] L. P. Šilnikov, Sov. Math. Dokl. **8**, 102 (1967).

[35] L. P. Šilnikov, Math. USSR Sb. **10**, 91 (1970).

[36] B. Deng, J. Diff. Equations **102**, 305 (1993).

[37] E. Ott, C. Grebogi, and J. A. Yorke, Phys. Rev. Lett. **64**, 1196 (1990).

[38] I. B. Schwartz and I. Triandaf, Phys. Rev. A **46**, 7439 (1992).

[39] Z. Gills, C. Iwata, R. Roy, I. B. Schwartz, and I. Triandaf, Phys. Rev. Lett. **69**, 3169 (1992).

[40] R. Roy, T. W. Murphy, Jr., T. D. Maier, Z. Gills, and E. R. Hunt, Phys. Rev. Lett. **68**, 1259 (1992).

[41] A. Gavrielides and V. Kovanis (unpublished).

[42] T. A. Wettergren (unpublished).